

UNIVERSITY OF GENEVA

ASTROPHYSICS LAB REPORT

MAY 24, 2023

**Spectral and Timing Variability of Magnetized
Neutron Stars**

By:
SAMSON MERCIER

Supervised by:
C. FERRIGNO

Abstract

Magnetized neutron stars accreting from a companion star emit X-ray radiation that is strongly modulated with the spin phase. They are also variables on time scales from seconds to months. By analyzing the pulsed emission, it is possible to study the emission mechanism and its geometry in the vicinity of the neutron star, where extreme gravity and radiation conditions are present. By analyzing the variability on different time scales, it is possible to study how neutron stars interact with the surrounding medium to capture the material to be accreted. On the other hand, spectral analysis can provide valuable insight into the underlying physics of X-ray pulsars. In this astrophysical laboratory, we perform a comprehensive analysis of the timing variability and spectral properties of the famous X-ray pulsar Centaurus X-3. Our results indicate that the pulsations, and the accretion mechanisms, of Centaurus X-3, have an important dependence on energy. Furthermore, we characterized Cen X-3's cyclotron resonant scattering feature at 29.73 ± 0.15 keV, implying a magnetic field strength of 2.56×10^{12} G. During this APL, we developed a timing variability analysis pipeline that, although solely applied to Centaurus X-3, we hope will be used in the future to study various X-ray sources.

Contents

1	Introduction	3
2	The sources in our study and their properties	4
3	The NuSTAR mission	5
4	Methodology	5
4.1	Data Retrieval	5
4.2	Timing variability	6
4.2.1	Data Extraction	6
4.2.2	Orbital Correction	7
4.2.3	Concatenation	7
4.2.4	Epoch folding	7
4.2.5	Pulse Profile	7
4.2.6	Epoch folding search	8
4.2.7	Data Segmentation	9
4.2.8	Pulse Profile Matrix	9
4.2.9	Pulse Frequency Correction	10
4.2.10	Pulsed Fraction	10
4.2.11	Bootstrap Method	11
4.2.12	Removing Background	11
4.3	Spectral modelling	12
4.3.1	Data Extraction	13
4.3.2	Building Model	13
4.3.3	Fitting Model	14
5	Results & Discussion	15
6	Conclusion	16
7	Acknowledgments	17

1 Introduction

Neutron stars (NSs) are compact objects formed during the final evolutionary stage of stars with masses $M_* \geq 8M_\odot$. Besides black holes, neutron stars are the smallest and densest objects that have been observed, with densities of $\sim 10^{17} \text{ kg/m}^3$ and radii on the order of 10 km. NSs are produced from supernova explosions of high-mass stars and their ensuing gravitational collapse that compresses the core past the white dwarf density to that of atomic nuclei. NSs are mainly composed of neutrons, resulting from the combination of electrons and protons at high density. In such intense conditions, the electron degeneracy pressure and repulsive nuclear forces are the only forces opposing gravity, as the core can no longer support nucleosynthesis. Due to the lack of nuclear fusion, NSs will cool down over time. However, NSs can change their fate drastically either through accretion or collision. In either case, if the NS reaches the Tolman-Oppenheimer-Volkoff mass limit, which depends on the NS's unknown Equation of State, it will undergo another gravitational collapse, turning into a black hole (Kalogera & Baym, 1996).

Because of their short radii, we can infer from angular momentum conservation that NSs reach high rotational periods of order 1 ms at birth, later decaying to 1 – 10 s depending on their evolution along the $P\dot{P}$ -diagram (see e.g., Enoto et al., 2019). Paired with the intense currents in their interiors, NSs are endowed with high magnetic fields on the order of $10^{8-14}G$ ($\sim 10^8G$ for Low-Mass X-ray Binaries, $\sim 10^{12}G$ for High-Mass X-ray Binaries, and $\sim 10^{14}G$ for magnetars). As a result, studying NSs can help us gain insight into the physics of such extreme magnetic and gravitational fields.

During this APL, we will focus on studying pulsars, a type of NSs. These compact objects emit beams of radiation along their magnetic poles that sweep across the sky as the star rotates. We can distinguish two categories of pulsars:

1. Rotation-powered pulsars, also known as radio pulsars, were first discovered by British astronomers Jocelyn Bell Burnell and Antony Hewish in 1967 (Hewish et al., 1968). These pulsars are powered by rotational energy and gradually slow down over time through the emission of radiation and particles.
2. Accretion-powered pulsars, also known as X-ray pulsars, emerge from binary star systems and remain in said systems, accreting matter from the secondary (van den Heuvel, 1973). In these regimes, accreted gas from the companion's stellar wind is channeled to the NS's poles by the intense magnetic field. This creates an accretion column that is heated to temperatures on the order of several keV and radiates in the X-ray. The footprint of the accretion streams creates an X-ray "hotspot" on the NS's surface. The combined radiation by these features moves in and out of the telescope's field of view as the NS rotates, giving rise to X-ray pulses.

Studying these X-ray pulses gives us the opportunity to directly probe the NS's accretion geometry, while their magnetic field can be characterized by spectral analysis. On a NS's spectrum, described by a Compton continuum at first order, we can observe cyclotron resonance scattering features (CRSFs). CRSFs are due to the resonant scattering of photons by electrons in the NS's strong magnetic field. They are inherently linked to the discrete energy levels of the cyclotron orbits of electrons in magnetic fields, also known as Landau levels (Landau, 1930). The centroid energy of the CRSFs is related to the magnetic field by:

$$E_n = \frac{n}{(1+z)} \frac{eB\hbar}{m_e c} \approx \frac{n}{(1+z)} 11.6 * B_{12} \text{ keV} \quad (1)$$

where n is the Landau level considered, z is the gravitational redshift, m_e is the electron rest mass, B is the magnetic field measured in Gauss, and $B_{12} = B/10^{12}G$. Therefore, we can measure the magnetic field strength of NSs from the centroid energy E_n of the CRSFs present in their spectrum.

In this project, we perform a timing variability analysis. We developed techniques to determine the spin period, make pulse profiles for the neutron star at various energy ranges, and from those, compute the pulsed fraction as a function of energy. We perform also a spectral analysis. We adopt a pre-existing pipeline made to fit the spectra of X-ray binaries with diverse models and identify the CRSFs. By comparing the results of the two analyses we can constrain the physical properties and accretion mechanisms of various sources. For this APL, we focused on the High-Mass X-ray pulsar Cen X-3, exploiting data collected by the NuSTAR mission (Harrison et al., 2013).

We detail the properties of the main source in our study, Cen X-3, in section 2. We give some background information on the NuSTAR mission in section 3. The methods required to reach our goals are described in section 4. We present the spectrum, pulse profile, and pulsed fraction as a function of energy for the source of interest, and we discuss the implications of these results in section 5.

2 The sources in our study and their properties

Cen X-3 is a well-studied X-ray pulsar that has been observed with all X-ray space-based satellites launched over the past 50 years. Cen X-3 is a prime candidate for observation as it is a persistent bright source (although it shows strong long-term flux variation, see Paul et al., 2005), with a prominent CRSF around 30 keV (for a review, see Tomar et al., 2021). Cen X-3 belongs to a binary system located at a distance of 5.7 ± 1.5 kpc (Thompson & Rothschild, 2009), composed of a NS with a mass of $1.2 \pm 0.2 M_\odot$ and an O6-8 III supergiant star with a mass of $20.5 \pm 0.7 M_\odot$ (Ash et al., 1999). Cen X-3 is an accreting high-mass X-ray binary with an orbital period of 2.1 days and a spin period of ~ 4.8 s (Schreier et al., 1972). The binary system has an important inclination, such that the pulsar is eclipsed by the companion star for approximately 20% of its orbit (Suchy et al., 2008). The mass transfer occurs according to a Roche lobe overflow, which has led to the creation of an accretion disk around Cen X-3 (Tjemkes et al., 1986). The continuum of Cen X-3's spectrum is well-described by a cutoff power law, and a number of its other spectral properties have been successfully characterized. This includes the presence of strong full and partial absorption due to dense clumps of materials passing through the line-of-sight to the NS, and three fluorescence lines arising from regions of varying distance and ionization on the line-of-sight (Suchy et al., 2008; Ebisawa et al., 1996). Despite the abundance of data and studies performed on Cen X-3, some components still have unclear origins, such as the “10-keV” feature pointed out by Suchy et al. (2008); Thallhammer et al. (2021).

Understanding the mechanisms relating spectral features to the accretion columns of X-ray pulsars such as Cen X-3 is still an active area of research. It requires complex modeling of numerous physical phenomena such as radiative transfer and plasma deceleration, and can only be tackled numerically (Wang & Frank, 1981; West et al., 2017). These simulations can be quite computationally demanding, which results in most studies relying on empirical descriptions of spectral properties of X-ray binaries. Nonetheless, a few attempts have been made to connect observations with the physical properties of accretion columns, such as Ferrigno et al. (2009); Wolff et al. (2016).

3 The NuSTAR mission

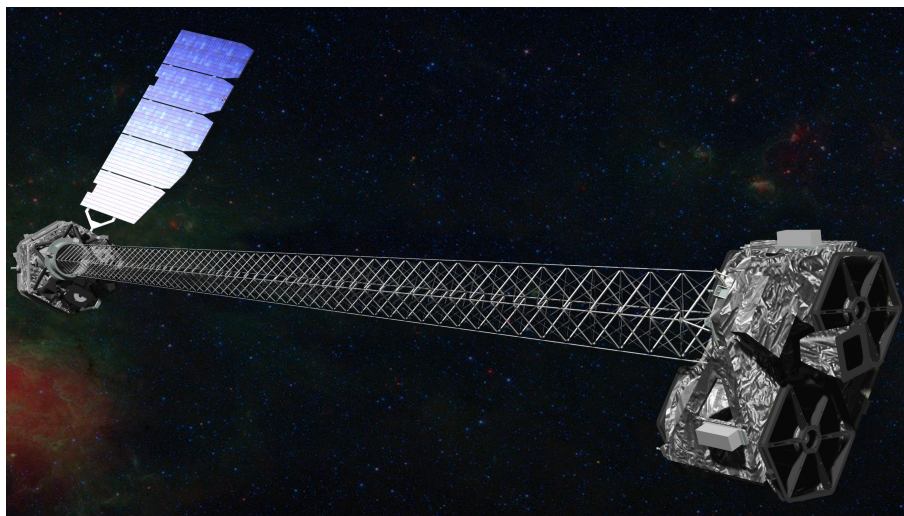


Figure 1: An artist view of NuSTAR aircraft (Credits, NASA Harrison et al., 2013).

The Nuclear Spectroscopic Telescope Array (NuSTAR) was launched on 13 June 2012. It is positioned on a geocentric near-equatorial orbit with inclination 6.027° and period 96.8 minutes. Thanks to its nested Wolter Type-I multi-coated optics, NuSTAR is the first hard X-ray-focusing telescope to operate in the 3 – 79 keV energy range. It is composed of two identical co-aligned grazing telescopes that focus X-ray photons on two Focal Plane detector Modules (abbreviated as FPMA and FPMB hereafter). Each module housing a 32×32 0.6-mm CdZnTe pixel detector, with an energy resolution of 400 eV at 10 keV and 900 eV at 60 keV (FWHM), is encapsulated in a CsI anti-coincidence detector.

In order to compensate for the low effective area due to the grazing incidence configuration of the conical Wolter Type-I mirrors, NuSTAR required an important focal length of about 10m to collect high-energy photons. This was achieved by separating the telescope's optics from the detector modules with an expandable composite mast. Unfortunately, the mast is not stiff enough to maintain a precise alignment between the detectors and the optical system. To take into account the changes in position resulting from the mast's movement, NuSTAR is equipped with an aspect/metrology system. The information from this system, composed of four star trackers and two metrology units, is used to correct for imperfections in the alignment and reconstruct the position of each photon.

Further details on NuSTAR's instruments and structure are provided by Harrison et al. (2013).

4 Methodology

4.1 Data Retrieval

We developed our pipeline using observations of the X-ray pulsar Cen X-3 made with NuSTAR from 17:30:49 UT on 22 October 2015 to 04:01:11 UT on 23 October 2015. Data are publicly avail-

able at NASA’s High-Energy Astrophysics Science Archive Research Center¹ (HEARSAC). These observations were made with an exposure time of 21.4 ks (OBSID: 30101055002, Pottschmidt et al., 2018; Thalhammer et al., 2021; Tomar et al., 2021; Alonso-Hernández et al., 2022). The source data was extracted by C. Ferrigno after processing the raw NuSTAR data with the standard pipeline. Background regions away from the source were also determined and processed accordingly to allow for the characterization and removal of background from the source data.

4.2 Timing variability

Our timing variability analysis aims at characterizing the neutron star’s pulse profile and pulsed fraction in a range of energies. In the sections below, we highlight the different steps needed to obtain these results. The pipeline developed during this work and utilized to perform the timing variability analysis of different sources is publicly available at <https://renkulab.io/gitlab/carlo.ferrigno/ap-lab-i-2022>. In particular, all the functions for our analysis have been defined and implemented in the Jupyter notebook `DayM.ipynb` and the Python module `Important.Functions.py`.

4.2.1 Data Extraction

The essential parts of X-ray data are the ‘event files’, containing the list of detected photons with their relevant parameters. These are stored in the ‘Flexible Image Transport System’ (FITS) format. From the .FITS files containing the processed NuSTAR events, we extract three arrays: the Event Arrival Times (EATs), their Pulse Invariant (PI) energies, and the Good-Time Intervals (GTIs). A comprehensive explanation of these quantities is provided below.

Optical and IR telescopes measure source flux during their observations, thanks to the abundance of photons in these wavelength ranges. In contrast, the exponentially decreasing number of high-energy photons constrains X-ray telescopes to measure individual photon detections, known as events. The EATs correspond to the times, with respect to a reference Modified Julian Date, at which photons were detected.

X-ray telescopes initially measure photon energy as a Pulse Height Amplitude (PHA). PHA values are related to the number of electrons generated in the detector by a constant, called the gain. A conversion is then made from PHA to PI, to correct for the gain and store values proportional to the photon energy. For NuSTAR, the PI columns are set to 40 eV per channel. The photon arrival times can be separated into two different sets: the GTIs and the Bad-Time Intervals (BTIs). GTIs are time intervals along the scientific exposure that can be safely exploited for scientific analysis because they have been treated for contaminating effects that might occur during the observation. These effects may include the passage of the spacecraft inside the South Atlantic Anomaly, heavy contamination from the background, telemetry gaps, occultation from the telescope’s orbit around Earth, or instrumental malfunction. In contrast, BTIs are intervals of time during which data cannot be collected.

Even during time intervals flagged as ‘good’, the detectors are subject to some dead time. These correspond to the time needed for an instrument to process an event and get ready for the next one. Dead time may also result from the anti-coincidence shield detecting a cosmic ray hit or other instrumental effects. In most current X-ray missions, including NuSTAR, dead time is non-paralyzable, meaning the instrument does not accept new events during these intervals. This also leads to a loss of information if the source’s photon emission rate is higher than the dead time rate. Although dead time intervals are approximately energy independent and, as such, have no impact on the spectral variability analysis, their effect on timing variability analysis is

¹<https://heasarc.gsfc.nasa.gov>

more problematic: dead time distorts the periodogram. Bachetti & Huppenkothen (2018) have introduced an efficient method to model dead time intervals and decorrelate them from the EATs in the GTIs. Their methods were not incorporated into our pipeline, as they are outside the scope of this project.

We extract the three quantities described above for each of the NuSTAR detectors. We note that the GTIs for FPMA and FPMB are identical, and as a result, we pursue our analysis solely with the FPMA’s GTIs.

4.2.2 Orbital Correction

The EATs are initially expressed in the local satellite time frame and must be converted to Barycentric Dynamical Time (TDB) frame, whose spatial origins lie at the Solar System barycenter. The TDB correction is done preemptively to the start of our analysis the processing pipeline. We also carry out an orbital correction to account for the gravitational interactions between the neutron star and its massive companion ($\sim 10 - 100 M_{\odot}$). To do so, we use the `get_orbital_correction_from_ephemeris_file` function built into the `Stingray`² package (v1.0, Huppenkothen et al., 2019b; Huppenkothen et al., 2019a; Bachetti et al., 2022), paired with the source orbital parameters provided by NASA’s National Space, Science and Technology Center Gamma-Ray Astrophysics Team³. Overall, two changes of reference frame are made to the photon arrival times: first from the spacecraft to the TDB reference frame, and then to the line of nodes of the binary system.

4.2.3 Concatenation

We concatenate the EATs and energy data for FPMA and FPMB before starting the core of our analysis.

4.2.4 Epoch folding

Epoch folding (also known as phase folding) is an essential tool for pulsar astronomy, which is used extensively in the following methods. It consists in cutting up the EATs in intervals of pulse period size and summing them in phase according to the following equation:

$$(t - t_{\text{ref}}) \times \nu_{\text{pulse}} \bmod 1 = \phi \quad (2)$$

Where ν_{pulse} is the pulse frequency, ϕ is the phase, and t_{ref} is a reference time in Modified Julian Days. For simplicity, we set t_{ref} to the start time of observations. To perform epoch-folding, we use the `phase_fold` function defined in our pipeline.

4.2.5 Pulse Profile

In astronomy, light curves reveal the photon flux, or photon count in the case of X-ray instruments, as a function of time. A pulse profile is a light curve that has undergone epoch-folding. To make a pulse profile from the EATs, we use the `make_lightcurve` function from the `Lightcurve` sub-package in `Stingray`. This routine takes as input the photon arrival times and time resolution over which we bin the EATs to calculate the photon counts. An example pulse profile for Cen X-3 is shown in Figure 2.

²<https://docs.stingray.science>

³<https://gammaray.nsstc.nasa.gov>

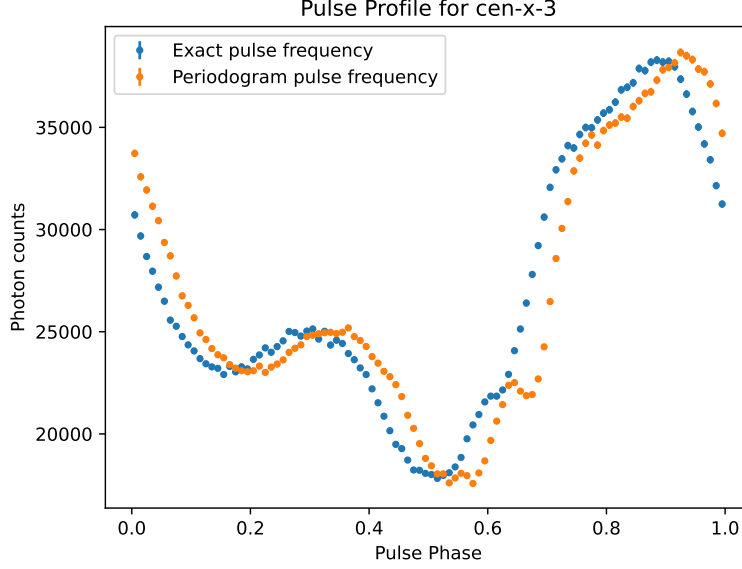


Figure 2: Pulse Profile of Cen X-3. The blue points correspond to the pulse profile calculated with the ‘true’ pulse frequency, obtained from our periodogram and Epoch folding search routines combined (detailed in Section 4.2.4). The orange points correspond to the pulse profile obtained solely from the periodogram. The difference between the two pulse profiles highlights the need for high-precision determination of the pulse frequency using an epoch folding search algorithm.

4.2.6 Epoch folding search

In order to detect periodicity in the EATs and find ν_{pulse} we use a periodogram and an epoch-folding search algorithm. We obtain a first guess of the pulse frequency by computing the Lomb-Scargle periodogram on the EATs from the routine **LombScargle** found in the **time-series** sub-package of **Astropy**⁴ (v5.1, Astropy Collaboration et al., 2013, 2018, 2022). Using **epoch_folding_search**, we can then probe a range of frequencies around this first estimate and refine our value of the pulse frequency. With this method, we compute the fit statistic on a given pulse profile as a function of the epoch-folding frequency. If the fit statistic is above a certain threshold, then the corresponding frequency is accepted as the pulse frequency. For this task, we use the **epoch_folding_search** routine from the Stingray package which applies the following statistic:

$$SSQ = \sum_i \frac{(P_i - \bar{P})^2}{\sigma^2} \quad (3)$$

with SSQ the sum-squared error which follows a χ^2 distribution, P_i the count value of the i -th bin in the pulse profile, \bar{P} the mean count, and σ the standard deviation of the counts. Because the photon counts follow a Poisson distribution, the standard deviation is $\sigma = \sqrt{N}$, with N the number of counts in each bin.

Getting a precise measurement of the pulse frequency is essential as the pulse profile’s topology is highly dependent on the folding frequency. If high precision is not achieved, the epoch folding

⁴<https://www.astropy.org>

will change slightly for each bin and the pulse profile will not reflect the true pulsation of the source. This effect is shown in Figure 2 where the difference in our pulse frequency determination methods leads to a phase offset of the pulse profile. Although our pulse frequency correction routine (see Section 4.2.9) could correct the pulse frequency value obtained solely from the periodogram, meaning the epoch folding search could be ignored, it is important to note that we are studying Cen X-3, a bright source. For dimmer sources, it is advantageous to perform the epoch folding search as their periodogram is contaminated by their low signal-to-noise ratio. For further information on the different periodicity searching methods available in the Stingray package, see Huppenkothen et al. (2019b).

4.2.7 Data Segmentation

We are interested in plotting the epoch-folded pulse profiles for different energy values. To do so, we segment the event arrival times according to the energy ranges we consider. The segmentation can be done either with energy bins of fixed length or with bins of logarithmic length. The latter is prioritized for the remainder of our analysis, as the number of X-ray photons tends to decrease exponentially with energy. We also decided to segment the arrival times linearly with fixed time intervals. Plotting the pulse profiles for these segments helps ensuring that the orbital correction and epoch-folding search steps worked as intended. If this is not the case, the pulse frequency correction routine described in section 4.2.9 will be applied. A more detailed explanation of our segmenting process can be found in the `segment_energywise` and `segment_timewise` functions of our pipeline.

4.2.8 Pulse Profile Matrix

We create a matrix of pulse profiles for the segmented EATs. For each segment, we epoch-fold the EATs and create a pulse profile with respect to the pulse frequency calculated in section 4.2.6. We also plot an n -th order sinusoidal model to each individual pulse profile where n , the number of harmonics used to describe a pulse profile, is obtained from our custom optimization function, `find_optimal_order`. To find the optimal model order n , we iterate over values of n ranging from 1 to $l/2$, where l is the size of the pulse profile's array. By calculating a fit statistic for each order we can determine which model best describes the given pulse profile. For each iteration i , we obtain the sinusoidal model counts $C_{m,i}$ from our custom function `model_pulse`. This function has for input the pulse profile time and count arrays t and C , and calculates $C_{m,i}$ according to the following equations:

$$C_{m,i} = \frac{1}{L} (0.5A_0 + \sum_{k=1}^i A_k \cos((2\pi t) * k + \phi_k)) \quad (4)$$

with A_k and ϕ_k defined as follows:

$$A_k = \sqrt{X_k^2 + Y_k^2} \quad (5)$$

$$\phi_k = \arctan 2\left(\frac{Y_k}{X_k}\right) \quad (6)$$

X, Y are arrays describing the real and imaginary parts of the Fourier transform of the provided counts:

$$FFT(C) = X + iY \quad (7)$$

and L , the normalization constant, is the length of X .

For each iteration, we compute the χ^2 statistic and the corresponding survival function (obtained from `scipy.stats.chi2.sf`). When the survival function surpasses a confidence level, provided as input to the `find_optimal_order` function, we stop iterating and use the associated sinusoidal order to model the pulse profile. We implement a fail-safe system in the event that the survival function never reaches the provided confidence level or if the sinusoidal model enters an overfitting regime (set to $n > 10$). In our fail-safe system, the first order that yields a negative difference in consecutive survival function values is chosen as the optimal order. By doing so, we ensure our model corresponds to a local maximum of the survival function and will not overfit the data. It may occur that our optimization routines described above output a first-order sinusoidal model. However, we empirically found that a second-order sinusoidal model is a better fit for pulse profiles. As a result, we increase the order to $n = 2$ in the case that our two previous routines output $n = 1$.

Example pulse profile matrices are shown in Figures 9 and 10. Further explanation of each step described above can be found in our `pulse_profile_matrix` function.

4.2.9 Pulse Frequency Correction

As mentioned in section 4.2.7, the accuracy of our orbital correction and epoch-folding search routines can be evaluated by plotting the pulse profile matrix from time-segmented data. In particular, we expect all the pulse profiles to have compatible phase offsets across the matrix. This can be verified by plotting the phase of the first harmonic for each pulse profile. If the profiles indeed have identical offsets, the first harmonic phases should lie along a horizontal line (shown in Figure 11). In our case, the pulse period, and as a result, the first harmonic phases, shift with time (shown in Figure 12). As a result, we must include a time derivative of the pulse frequency in our epoch folding algorithm defined in Section 4.2.4. By fitting a 2^{nd} order polynomial, we can extract linear and quadratic terms and correct for the variations in the first harmonic phase, by updating the epoch folding function as follows:

$$(t - t_{\text{ref}})(\nu_{\text{pulse}} - \nu_{\text{correction}}) - 0.5\dot{\nu}_{\text{pulse}}(t - t_{\text{ref}})^2 \bmod 1 = \phi \quad (8)$$

where $\nu_{\text{correction}}$ and $\dot{\nu}_{\text{pulse}}$ are the best-fit linear and quadratic terms of the 2^{nd} order polynomial, respectively.

4.2.10 Pulsed Fraction

From each pulse profile in the matrix, we extract a value for the pulsed fraction. The definition of this quantity varies among authors, here we use the pulsed signal's root mean square (RMS). The RMS of a given pulse profile can be calculated in the frequency domain using Parseval's theorem:

$$RMS = \frac{1}{A_0} \sqrt{\sum_k^n A_k^2} \quad (9)$$

where n is the order of the sinusoidal model used to describe the considered pulse profile, and A_k is defined according to equations 5 and 7. We then make a plot of the pulsed fraction against photon energy. The horizontal bars shown in Figure 4 correspond to the energy range over which the pulsed fraction was computed. We calculate the energy range with $0.5 * (\max(E_m) - \min(E_m))$, where E_m is the energy array of the m -th pulse profile, obtained from our data segmentation routine detailed in section 4.2.7. The uncertainty on the pulse fraction is obtained from our bootstrapping method, described in section 4.2.11.

The pulsed fraction plot gives us information on how photons are emitted in the accretion column of the neutron star and when compared with the spectral analysis described in section 4.3, may help us to infer the physical properties of the X-ray binary system.

4.2.11 Bootstrap Method

In order to estimate the uncertainty of quantities such as the pulsed fraction or the phase of the first harmonic for each pulse profile we implement a bootstrapping method. Since the counts in each pulse profile follow a Poisson distribution, we can create N distinct realizations of a pulse profile by sampling a Poisson distribution. The uncertainty on a given statistic of the pulse profile, such as the RMS, can then be approximated by its standard deviation across all N Poisson realizations. Our functions **bootstrap_generate** and **bootstrap_total** generate the N realizations and calculate the standard deviation of an input statistic, respectively. We show simulations of a pulse profile using our **bootstrap_generate** function in Figure 3. An example Pulsed fraction plot including errors on the RMS calculated through our bootstrap method can be found in Figure 4.

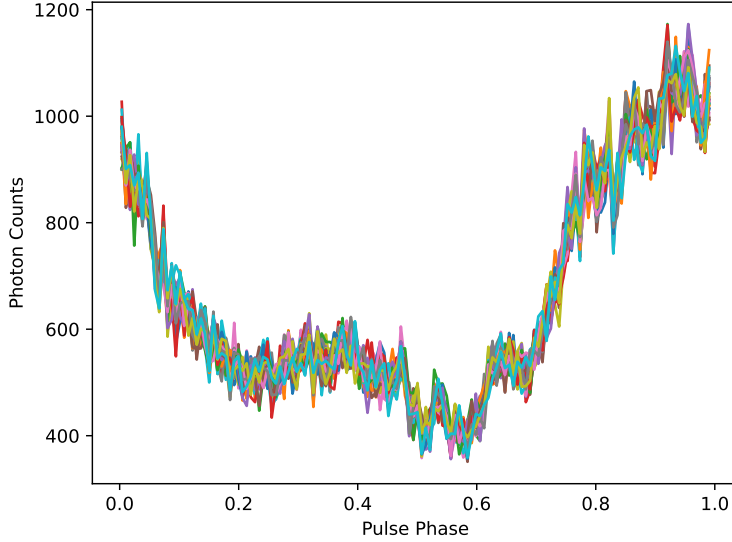


Figure 3: 30 Poisson simulations of a pulse profile. Each colored line corresponds to one realization of the pulse profile considered. Statistics such as the RMS can be calculated on each simulation.

4.2.12 Removing Background

The event files contain photons from both the source and background. As a result, we must remove the background in order to have a pulsed fraction plot that solely describes the source. We have also data from a region of the sky where the source was not present which we use to characterize the background. As described in the previous section, we extract the EATs, associated energies, and GTIs, apply an orbital correction to the EATs, concatenate the data

of both NuSTAR detectors, segment the background data with respect to the photon energies, and generate a pulse profile matrix. We then subtract the average background energy counts from the source energy counts in each pulse profile. Finally, we plot the background-subtracted pulsed fraction as a function of energy according to the methods outlined in sections 4.2.10 and 4.2.11. We show the pulsed fraction with and without background contamination in Figure 4. We note that the source signal, as detected by the instruments, is more affected by background at high energies where the emissions decay exponentially and the effective area is reduced.

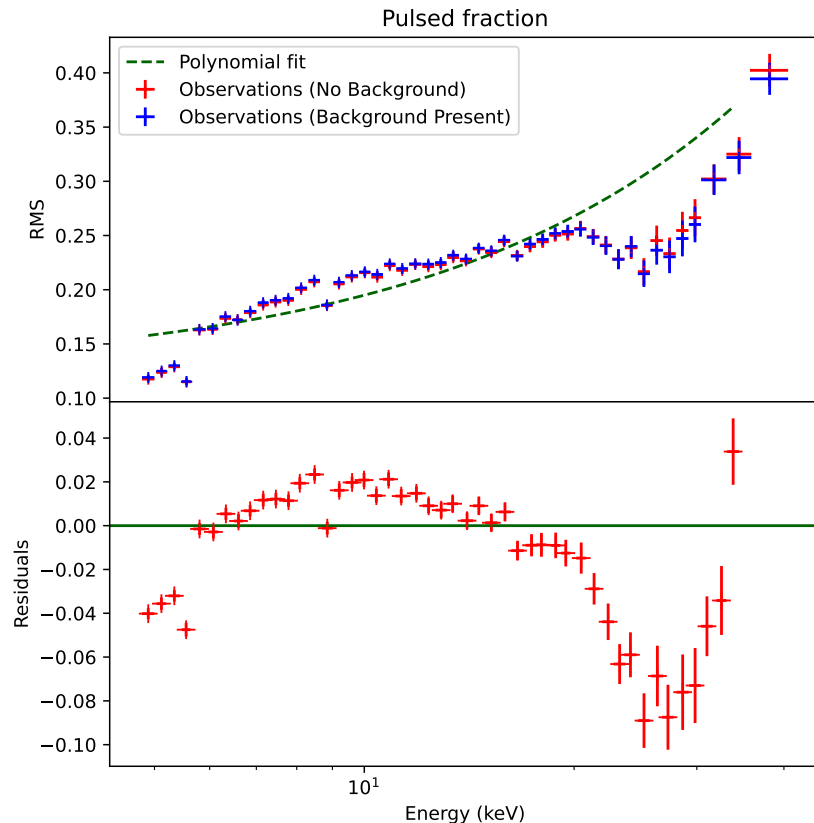


Figure 4: Pulsed Fraction of Cen X-3. *Top panel:* We plot the RMS of each pulse profile as a function of their corresponding energy. The blue crosses represent the RMS obtained from the source file while the RMS values for the red crosses have undergone background correction. The green dashed line is a 1st order polynomial fit to the background-corrected pulsed fraction with a Levenberg-Marquardt algorithm. *Bottom panel:* Corresponding residuals for our polynomial fit.

4.3 Spectral modelling

Our spectral analysis aims at characterizing the neutron star’s spectral distribution with a variety of models. The associated best-fit parameters provide information on the pulsar’s physical properties. The pipeline used to carry out the spectral analysis was provided as teaching material.

4.3.1 Data Extraction

From the source .FITS files, we extract the photon counts in each PI channel and their corresponding energies. To correctly model the source spectrum, we also make use of a Redistribution Matrix File (RMF) and an Ancillary Response File (ARF). These files provide information on the energy resolution and the energy-dependent variations of photon counts for a given instrument.

The RMF is a dimensionless matrix relating incident photon energy to the associated event's PHA. This matrix informs us of the probability that a photon of a given energy is registered in the appropriate spectral channel. The ideal RMF would give a one-to-one mapping between PHA and photon energy, corresponding to a diagonal matrix. In practice, we see significant contributions from off-diagonal terms due to detector imperfections e.g. CCD channel overflow. The RMF helps characterize the energy resolution of detectors.

The ARF describes the effective area, and by extension, the photon counts as a function of energy for a particular observation. It encapsulates the telescope's geometric collecting area and the energy-dependent efficiencies of the mirrors, and detectors used. Because of detector non-uniformities and vignetting, the ARF is dependent on the source's position on the detector. For telescopes where dithering is present, the source will sample different areas of the detector, and as a result, the source's pointing history must be considered when making the ARF. NuSTAR's ARF is plotted in Figure 5 and computed by their pipeline.

4.3.2 Building Model

We build a model to describe the observed spectrum. Selecting the right model components is essential as we will be drawing conclusions on the properties of the binary system from their best-fit parameters. All components used for our analysis are taken from the X-ray Spectral Fitting Package⁵ (`xspec` v12.13.0, Arnaud, 1996), available in NASA's HEARSAC Xanadu X-ray Astronomy Data Analysis Software. The components can be distinguished into additive and multiplicative families. Additive models describe the baseline spectrum of an X-ray source while multiplicative models modify the distribution by an energy-independent factor. Convolution and mixing models can also be added to perform more sophisticated operations. The basic model we use to characterize the spectrum of a source is:

$$\text{TBabs} * \text{highcut} * \text{pegpwlw}$$

$$\text{pegpwlw} : A(E) = K * E^{-\alpha} \quad (10)$$

with $K = \int_{E_{\min}}^{E_{\max}} A(E) dE$

$$\text{highcut} : M(E) = \begin{cases} \exp(\frac{E_c - E}{E_f}) & E \geq E_c \\ 1 & E \leq E_c \end{cases} \quad (11)$$

$$\text{TBabs} : M(E) = \exp n_H \sigma_{\text{PE}}(E) \quad (12)$$

with $\sigma_{\text{PE}}(E)$ photoelectric plus dust cross section.

`pegpwlw` is an additive model for a power law with pegged normalization, `highcut` is a multiplicative model for a high-energy cutoff and `TBabs` is a multiplicative model for a Tuebingen-Boulder Interstellar Medium model. We can separate the parameters from each component into frozen and free parameters, which will be set or fit for, respectively. In our basic model, the frozen parameters are E_{\min} , E_{\max} and the free parameters are K , α , E_c , E_f , and n_H . A detailed description of each parameter is provided in the `Xspec` documentation. Although our

⁵<https://heasarc.gsfc.nasa.gov/docs/xanadu/xspec>

base model is a good first-degree approximation of the spectrum of X-ray pulsars, we must add components to our basic implementation described above in order to correctly characterize the complex spectral distribution of these objects. The selection process for these components requires years of experience and intuition in the field of X-ray astrophysics and as a result, was not tackled during this project. To the basic model above, we add Gaussian lines to describe the iron emission around 6.4 keV, multiplicative `gabs` absorption features to describe the CRSF and fudge the cutoff, and a partial covering absorption to describe the diffusion in the supergiant star clumpy wind. The final model is `TBabs*pcfabs*gabs*gabs*(pegpwlw+gaussian+gaussian)`. The models used are provided in Tables 1 and 2, along with their best-fit parameters.

4.3.3 Fitting Model

Each model is fit to the data with a Goodman-Weare Markov Chain Monte-Carlo (MCMC) algorithm from the `pyxmmas` package. Users can choose between three priors for the free parameters: uniform, gaussian, or Jeffreys priors. The prior bounds for each free parameter are set in advance and provided as input to the MCMC. The `pyxmmas` MCMC algorithm can be run with a custom number of walkers, burn-in steps, and production steps, which helps evaluate and optimize the convergence of parameter chains. The spectra of both detectors are fit simultaneously so that a single set of best-fit parameters is output. The uncertainties on the model parameters are determined by sorting the chain and taking a central percentage of the values based on a given confidence interval (67.8% for our analysis). For each step of the MCMC, the χ^2 , BIC, and Cash statistics are computed and stored. The Cash statistic (Cash, 1979) corresponds to the maximum-likelihood-based statistic for Poisson data and is defined as:

$$C = 2 \sum_{i=1}^N (m_i t) - S_i + S_i \times (\ln(S_i) - \ln(m_i t)) \quad (13)$$

where t is the exposure time, S_i are the observed counts, m_i are the predicted counts, and N the total number of counts. The Cash statistic is favored for the likelihood maximization in the MCMC as both the χ^2 and the BIC statistics are biased when applied to data sampled from a Poisson distribution (e.g. photon counts). However, as long as $N \geq 30$ the Cash statistic is approximately equivalent to the χ^2 . All the sources we study have high photon counts, so we use the BIC and χ^2 to compare different models.

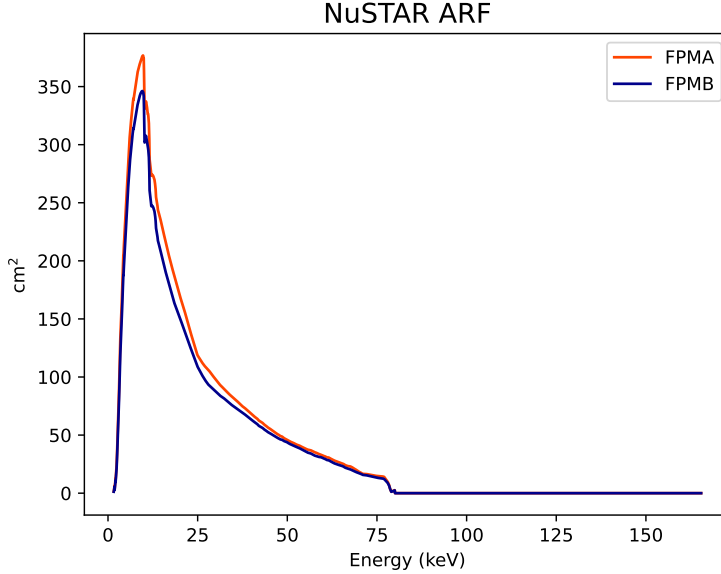


Figure 5: Ancillary Response Function of the NuSTAR telescope. The effective area for the FPMA and FPMB detectors is plotted as a function of energy in blue and orange lines, respectively. Although the ARF peaks at ~ 9.6 keV for both modules, the energy range covered is more important than for most current X-ray missions such as Chandra and XMM-Newton.

5 Results & Discussion

We present the pulsed fraction of Cen X-3 as a function of energy in Figure 4. We distinguish between the pulsed fractions with and without background correction in red and blue points, respectively. We note that background correction does not heavily impact the results as the data points with background correction are within 1σ of those without. We expect the pulsed fraction to increase as a function of energy, as the X-ray hotspot becomes narrower and the pulse profile becomes more modulated at higher energies. Subsequently, we fit a 1^{st} order polynomial to the pulsed fraction plot. From the residuals, we note that our fit does not describe certain features, especially the important dip around 30 keV. This corresponds to a CRSF that we attempt to characterize in our spectral analysis.

We present the pulse profile matrix of Cen X-3 in Figure 10. We note the presence of three peaks in the low energy regime, around 0.35, 0.65, and 0.95 phase. As we move to higher energies, the two smaller peaks disappear and the pulse profiles adopt a single-peak shape. Although the peaks around 0.35 and 0.95 phase have previously been observed by Suchy et al. (2008) and Raichur & Paul (2010), the narrowest peak at 0.65 phase was only recently observed by Tomar et al. (2021). Having multiple peaks in the pulse could indicate the presence of multiple magnetic poles on Cen X-3. The change in pulse profile shape as we move to higher energies, as seen in Figure 10, could be evidence of differences in accretion rates across these different poles. Although we can make hypotheses on the relation between accretion and pulse profile shape, the mechanisms underlying these results are not fully understood yet, as they require complex modeling of accretion columns and their interaction with the NS’s environment.

We present the observed spectrum of Cen X-3 fit with our base and improved models in

Figures 6 and 7. We list the parameter estimates for our basic and improved models obtained from the MCMC in Tables 1 and 2. From the $\Delta\text{BIC} = 6676$, it is evident that our improved model provides a better description of the Cen X-3 spectrum. The residuals for our base model present a peak around 6.5 keV and troughs at ~ 15 and ~ 30 keV. These features are not present in the residuals for our improved model, as we have modeled the peak at 14.42 ± 0.06 keV with a cutoff of the power law continuum and the trough at 29.73 ± 0.15 keV as a CRSF energy line. We note that our cyclotron energy measurements are within 2σ of the most up-to-date study performed by Tomar et al. (2021) using NuSTAR and within 1σ of their values found using Suzaku telescope data. Three iron emission lines at 6.4, 6.67 and 6.97 keV combine, due to NuSTAR’s low spectral resolution, to form the peak witnessed around 6.5 keV in our residuals. We modeled this feature through a gaussian line profile with line energy 6.356 ± 0.0081 keV and width 0.179 ± 0.015 keV. Other components presented in Table 2 such as TBabs and pcfabs, although essential to our analysis, pertain to effects along the line-of-sight and as such do not provide new information on the accretion geometry or magnetic field of Cen X-3. From our measurement of the CRSF, we find a magnetic field of $(1+z)B = 2.56 \times 10^{12}$ G. Such a powerful magnetic field was to be expected for Cen X-3 as it is categorized as a High-Mass X-ray Binary.

Component names	Parameter	Status	Fixed value/ Priors	Best-fit value
pegpwlw (A)	α	Free	$U(-3, 10)$	1.247 ± 0.003
	K (ergs/cm ² /s)	Free	$J(0, 10^{24})$	$(13533 \pm 44) \times 10^{-12}$
	E_{min} (keV)	Frozen	3	–
	E_{max} (keV)	Frozen	70	–
highecut (M)	E_c (keV)	Free	$J(10^{-4}, 10^6)$	14.424 ± 0.024
	E_f (keV)	Free	$J(10^{-4}, 10^6)$	8.288 ± 0.026
TBabs (M)	n_H (atoms cm ⁻²)	Free	$J(0, 10^6)$	$(11.66 \pm 0.09) \times 10^{22}$

Table 1: Initial and best-fit values for the component parameters in our base model applied to Cen X-3 NuSTAR data. We distinguish between Jeffrey priors (J) and uniform priors (U), and between additive (A) and multiplicative (M) model components. The errors on the best-fit values were computed from the MCMC chains (detailed in Section 4.3.3). Our basic fit does not include any components to model the CRSF. As a result, studying the residuals is a good way of detecting the presence or lack of CRSFs. The different model components and their respective parameters are described in Section 4.3.2 and in the **Xspec** documentation.

6 Conclusion

Timing variability and spectral analysis are important tools for studying X-ray pulsars. Timing variability allows for the determination of the pulsar’s rotation period and pulse profile, which can be used to infer the pulsar’s age and accretion geometry. Spectral analysis allows for the determination of the pulsar’s spectral properties, such as the presence of a blackbody component or a power law component, which can be used to understand the emission mechanism and the physical conditions in the pulsar’s environment. Together, these techniques provide valuable insights into the nature and evolution of X-ray pulsars. During this APL, we were able to characterize the CRSF and magnetic field strength of Cen X-3. The core of the APL was focused on

the development of a timing variability analysis pipeline. Although this pipeline has only been applied to the study of Centaurus X-3, we hope that it can help characterize other X-ray sources in the future.

Software: `Stingray`, `Astropy`, `Numpy`⁶ (v1.23.3, Harris et al., 2020), `Xspec`, `Scipy`⁷ (v1.9.1, Virtanen et al., 2020), `lmfit`⁸ (v1.1.0, Newville et al., 2014), `Matplotlib`⁹ (v3.6.0, Hunter, 2007)

7 Acknowledgments

S. M. would like to thank Dr. Ferrigno for his continuous support along this APL and his contagious enthusiasm for the study of neutron stars. His help during this APL, both in undertaking such an intricate coding project and understanding the complexities of high-energy astrophysics, was invaluable.

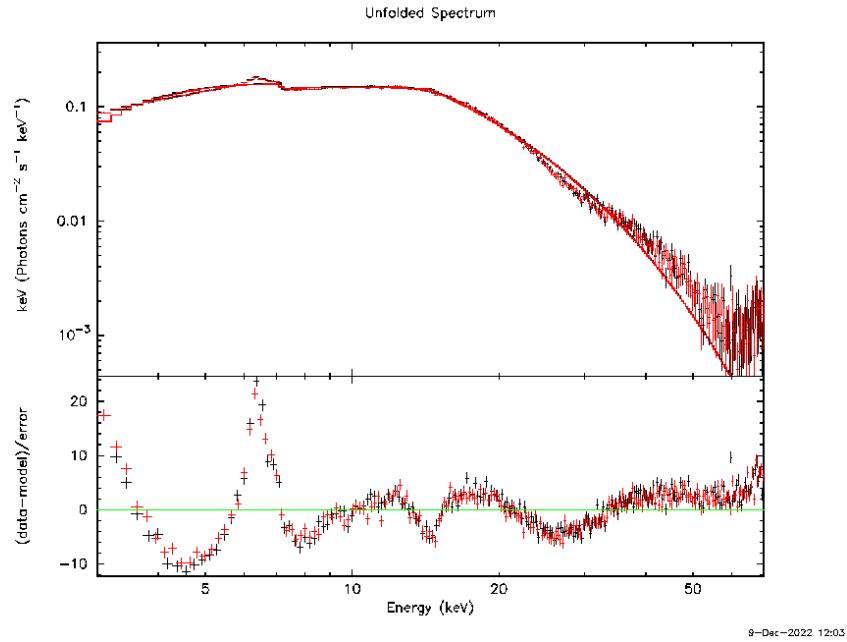


Figure 6: Cen X-3 spectrum fitted on the energy range 3 – 70 keV. *Top panel:* We plot the spectrum of Cen X-3 and our fitted base model. The red and black crosses are the observations with corresponding error bars, the red points represent the best-fit base model. The best-fit was found with BIC= 7483. *Bottom panel:* Corresponding residuals from the best-fit base model.

⁶<https://www.astropy.org>

⁷<https://scipy.org>

⁸<https://lmfit.github.io/lmfit-py>

⁹<https://matplotlib.org>

Component names	Parameter	Status	Fixed value/ Priors	Best-fit value
pegpwlw (A)	α	Free	$U(-3, 10)$	1.325 ± 0.018
	K (ergs/cm ² /s)	Free	$J(0, 10^{24})$	$(13683 \pm 113) \times 10^{-12}$
	E_{min} (keV)	Frozen	3	–
	E_{max} (keV)	Frozen	70	–
Gaussian1 (A)	E_L (keV)	Free	$U(0, 10^6)$	6.356 ± 0.008
	σ (keV)	Free	$J(0, 20)$	0.179 ± 0.015
	K	Free	$U(0, 10^{24})$	$(3.03 \pm 0.14) \times 10^{-3}$
Gaussian2 (A)	E_L (keV)	Frozen	6.97	–
	σ (keV)	Frozen	0	–
	K	Free	$U(0, 10^{24})$	$(5.8 \pm 0.6) \times 10^{-4}$
highcut (M)	E_c (keV)	Free	$J(10^{-4}, 10^6)$	14.42 ± 0.06
	E_f (keV)	Free	$J(10^{-4}, 10^6)$	9.81 ± 0.08
TBabs (M)	n_H (atoms/cm ²)	Free	$J(0, 10^6)$	$(2.6 \pm 0.7) \times 10^{22}$
gabs1 (M)	E_l (keV)	Free	$U(0, 10^6)$	29.73 ± 0.15
	σ (keV)	Free	$U(0, 20)$	5.32 ± 0.17
	δ	Free	$U(0, 10^6)$	6.59 ± 0.31
gabs2 (M)	E_l (keV)	Free	$U(0, 10^6)$	14.50 ± 0.07
	σ (keV)	Free	$U(0, 20)$	0.66 ± 0.06
	δ	Free	$U(0, 10^6)$	0.122 ± 0.011
pcfabs (M)	n_H (atoms/cm ²)	Free	$J(0, 10^6)$	$(40.5 \pm 2.6) \times 10^{22}$
	f	Free	$U(0, 1)$	0.549 ± 0.024

Table 2: Initial and best-fit values for the component parameters in our improved model applied to Cen X-3 NuSTAR data. We distinguish between Jeffrey priors (J) and uniform priors (U), and between additive (A) and multiplicative (M) components. The errors on the best-fit values were computed from the MCMC chains (detailed in Section 4.3.3). The different model components as well as their parameters are described in Section 4.3.2 and in the **Xspec** documentation.

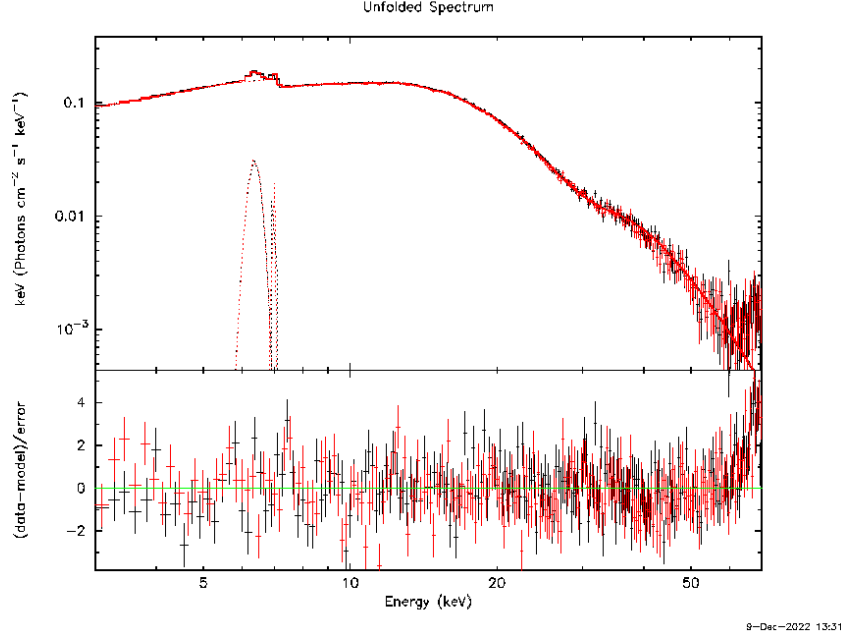


Figure 7: Cen X-3 spectrum fitted on the energy range 3 – 70 keV. *Top panel:* We plot the spectrum of Cen X-3 and our fitted improved model. The red and black crosses are the observations with corresponding errorbars, the red points represent the best-fit improved model. The best-fit was found with BIC= 806. *Bottom panel:* Corresponding residuals from the best-fit improved model.

References

- Alonso-Hernández J., Fürst F., Kretschmar P., Caballero I., Joyce A. M., 2022, *A&A*, 662, A62
- Arnaud K. A., 1996, in Jacoby G. H., Barnes J., eds, *Astronomical Society of the Pacific Conference Series Vol. 101, Astronomical Data Analysis Software and Systems V*. p. 17
- Ash T. D. C., Reynolds A. P., Roche P., Norton A. J., Still M. D., Morales-Rueda L., 1999, *MNRAS*, 307, 357
- Astropy Collaboration et al., 2013, *A&A*, 558, A33
- Astropy Collaboration et al., 2018, *AJ*, 156, 123
- Astropy Collaboration et al., 2022, *apj*, 935, 167
- Bachetti M., Huppenkothen D., 2018, *ApJ*, 853, L21
- Bachetti M., et al., 2022, *StingraySoftware/stingray: Version 1.0*, doi:10.5281/zenodo.6394742, <https://doi.org/10.5281/zenodo.6394742>
- Cash W., 1979, *ApJ*, 228, 939
- Ebisawa K., Day C. S. R., Kallman T. R., Nagase F., Kotani T., Kawashima K., Kitamoto S., Woo J. W., 1996, *Publications of the Astronomical Society of Japan*, 48, 425

- Enoto T., Kisaka S., Shibata S., 2019, Reports on Progress in Physics, 82, 106901
- Ferrigno C., Becker P. A., Segreto A., Mineo T., Santangelo A., 2009, A&A, 498, 825
- Harris C. R., et al., 2020, Nature, 585, 357
- Harrison F. A., et al., 2013, ApJ, 770, 103
- Hewish A., Bell S. J., Pilkington J. D. H., Scott P. F., Collins R. A., 1968, Nature, 217, 709
- Hunter J. D., 2007, Computing in Science & Engineering, 9, 90
- Huppenkothen D., et al., 2019a, Journal of Open Source Software, 4, 1393
- Huppenkothen D., et al., 2019b, ApJ, 881, 39
- Kalogera V., Baym G., 1996, ApJ, 470, L61
- Landau L., 1930, Zeitschrift fur Physik, 64, 629
- Newville M., Stensitzki T., Allen D. B., Ingargiola A., 2014, LMFIT: Non-Linear Least-Square Minimization and Curve-Fitting for Python, Zenodo, doi:10.5281/zenodo.11813
- Paul B., Raichur H., Mukherjee U., 2005, A&A, 442, L15
- Pottschmidt K., et al., 2018, in American Astronomical Society Meeting Abstracts #231. p. 243.11
- Raichur H., Paul B., 2010, MNRAS, 401, 1532
- Schreier E., Levinson R., Gursky H., Kellogg E., Tananbaum H., Giacconi R., 1972, ApJ, 172, L79
- Suchy S., et al., 2008, ApJ, 675, 1487
- Thalhammer P., et al., 2021, A&A, 656, A105
- Thompson T. W. J., Rothschild R. E., 2009, ApJ, 691, 1744
- Tjemkes S. A., Zuiderwijk E. J., van Paradijs J., 1986, A&A, 154, 77
- Tomar G., Pradhan P., Paul B., 2021, MNRAS, 500, 3454
- Virtanen P., et al., 2020, Nature Methods, 17, 261
- Wang Y. M., Frank J., 1981, A&A, 93, 255
- West B. F., Wolfram K. D., Becker P. A., 2017, ApJ, 835, 130
- Wolff M. T., et al., 2016, ApJ, 831, 194
- van den Heuvel E. P. J., 1973, Nature Physical Science, 242, 71

8 Appendix

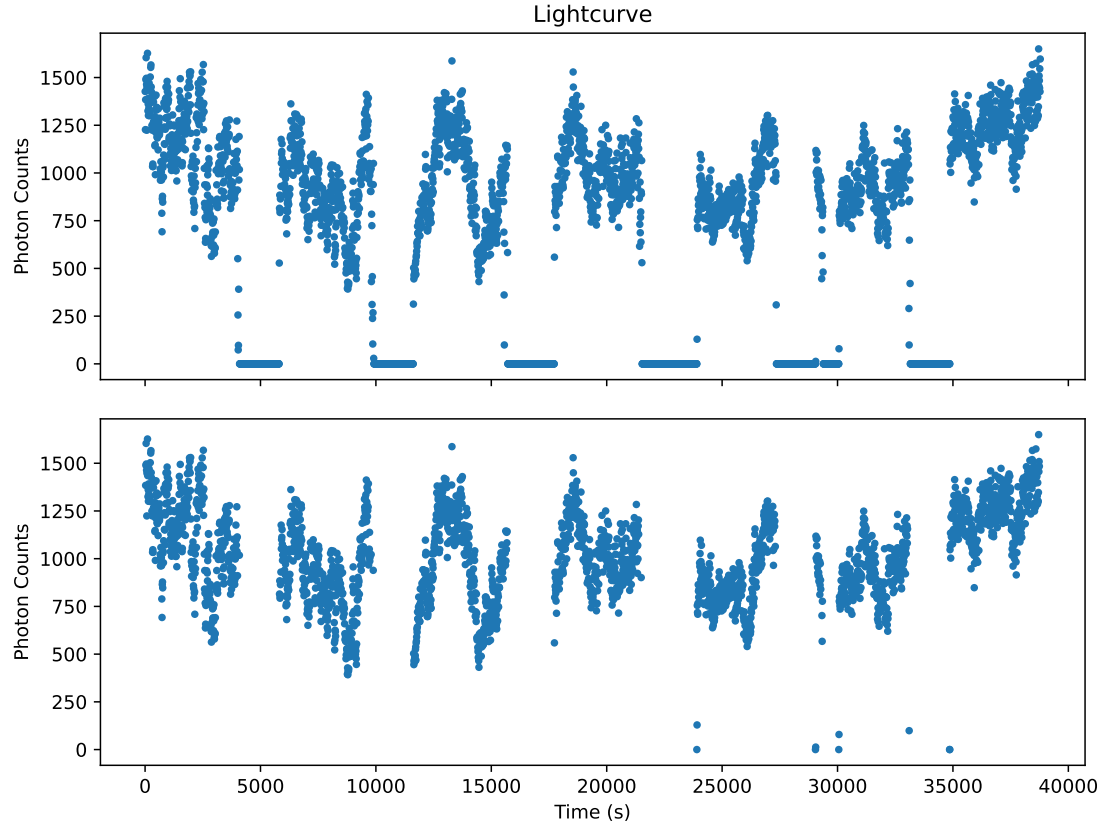


Figure 8: Lightcurve of Cen X-3. *Top panel:* Lightcurve containing BTIs and GTIs. The BTIs correspond to the sections with no photon counts, as the telescope did not collect data. *Bottom panel:* Lightcurve containing only GTIs. Both panels are plotted with respect to the start time of observations.

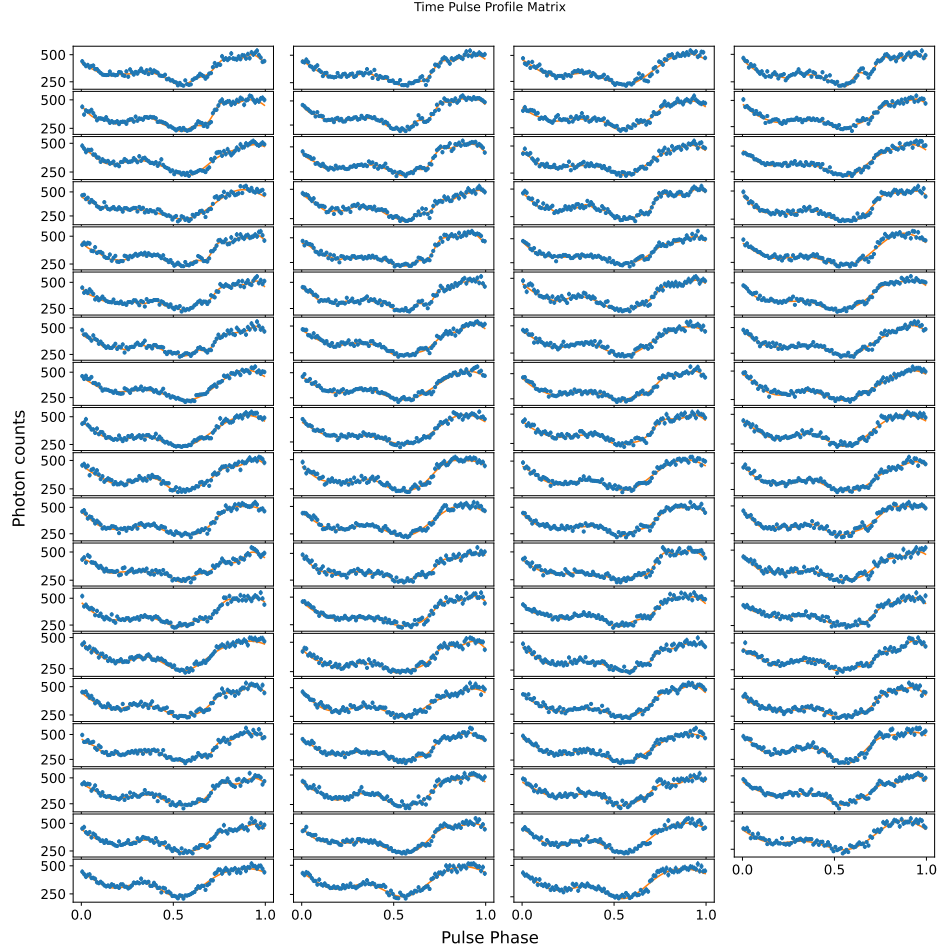


Figure 9: Time Pulse Profile Matrix of Cen X-3. The blue points correspond to the pulse profiles uniformly segmented in time. The orange line corresponds to the n -th order sinusoidal model fit to each individual pulse profile. The order n is determined with a χ^2 minimization routine detailed in Section 4.2.8. The consistent phase shift in each pulse profile confirms that our periodogram, epoch folding search, and pulse frequency correction steps were successfully executed.

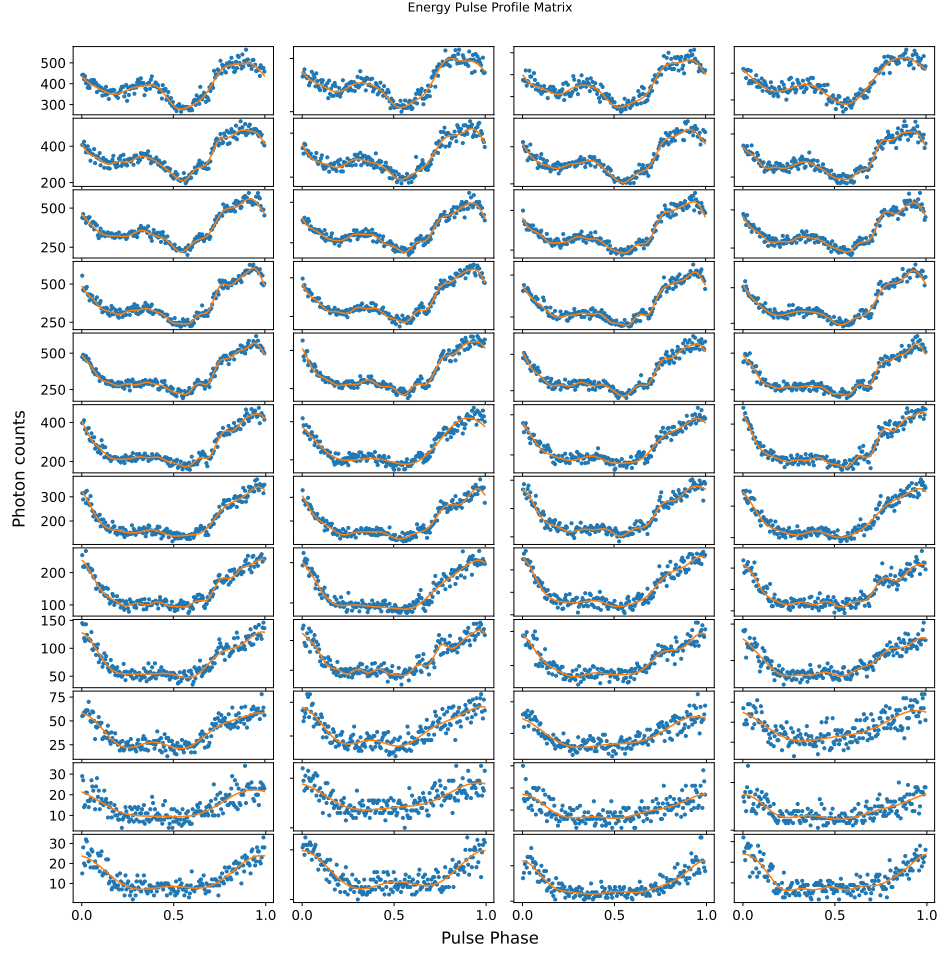


Figure 10: Energy Pulse Profile Matrix of Cen X-3. The blue points correspond to the pulse profiles segmented in energy with logarithmic bins. The orange line corresponds to the n -th order sinusoidal model fit to each individual pulse profile. The order n is determined with a χ^2 minimization routine detailed in Section 4.2.8. As expected the photon counts decrease exponentially with energy. Consequently, we implement logarithmic binning.

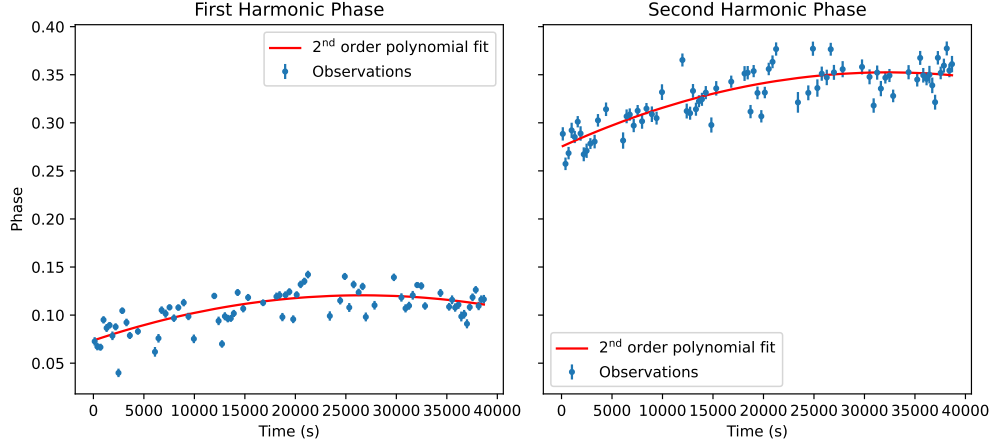


Figure 11: Plot of the first and second harmonics' phases as a function of time for Cen X-3, before the pulse frequency correction step detailed in Section 4.2.9. For each pulse profile in the Time Pulse Profile Matrix, we extract the phase of the first and second harmonic and plot them against the average time in each pulse profile. Both panels are plotted with respect to the start time of observations. As we can see the first harmonic phases do not fall along a horizontal line, so a correction to the pulse frequency must be applied..

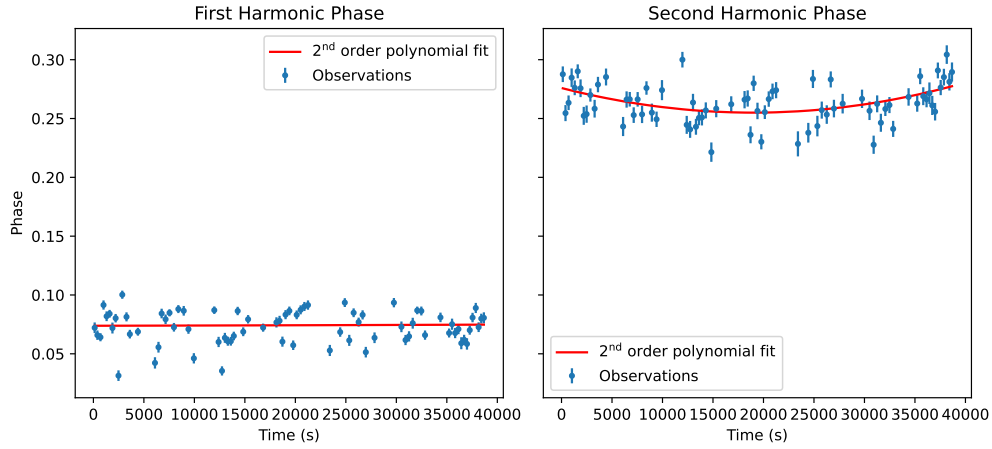


Figure 12: Plot of the first and second harmonics' phases as a function of time for Cen X-3, after the pulse frequency correction step. For each pulse profile in the Time Pulse Profile Matrix, we extract the phase of the first and second harmonic and plot them against the average time in each pulse profile. Both panels are plotted with respect to the start time of observations. If the pulse frequency were correct, the first harmonic phases should fall along a horizontal line, as is observed. If this is not the case, a pulse frequency correction routine must be implemented, as detailed in section 4.2.9. Although there is some variation in the second harmonic phase, corrections brought to these frequencies have a negligible effect.